Additive Manufacturing 39 (2021) 101885

Contents lists available at ScienceDirect

Additive Manufacturing

journal homepage: www.elsevier.com/locate/addma

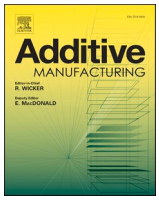

Research Paper

Investigating the dynamic compression response of elastomeric, additively manufactured fluid-filled structures via experimental and finite element analyses

Shwe Soe [a,*], Rhosslyn Adams [b], Mokarram Hossain [c], Peter Theobald [b]

[a] Department of Engineering, Design and Mathematics, University of the West of England, Bristol BS16 1QY, UK
[b] Cardiff School of Engineering, Cardiff University, CF24 3AA, UK
[c] Zienkiewicz Centre for Computational Engineering, College of Engineering, Swansea University, SA1 8EN, UK

ARTICLE INFO

Keywords:
Fluid-filled structure
Additive manufacturing
Dynamic compression
Smooth particle hydrodynamic
Visco-hyperelastic constitutive model

ABSTRACT

This study evaluates a fluid-filled, closed-cell lattice as a novel route to reducing peak acceleration in impact environments. A conical structure was designed and built using fused filament fabrication. One structure was manufactured hollow (100% air), another 70% filled with water (50% by height) and a third 100% water-filled. Peak acceleration was evaluated by performing 4.1 kg impacts at 1, 2, 3 m/s. Impacts were then simulated in shell and solid finite element analysis models, employing the smooth particle hydrodynamic method for the water and a or the surface-based fluid-filled cavity method for air. The air-filled, conventional closed-cell structures achieved the lowest peak accelerations at lower impact energies, however, water infill improved impact performance at higher energies. For low to medium impact energies, shell and solid modelling accurately simulated experimental trends, although the latter is more computationally expensive. Solid modelling is the only viable solution for scenarios achieving structural densification, due to the inaccuracies in shell-based models caused by the inter-surface penetrations. This work has demonstrated that fluid-filled structures provide a promising approach to reduce acceleration and so achieving enhanced protection, whilst also presenting a computational pathway that will enable efficient design of new and novel structures.

1. Introduction

Additive Manufacturing (AM) is a layer-by-layer build process that enables the realisation of geometrically complex structures. Recent development in AM hardware and software means builds can now achieve greater accuracy, finer resolution, better surface quality and improved mechanical properties [1–3]. Increasing capability and reducing cost means AM is now attractive to industry, creating market demand for new base materials [4–6]. Thermoplastic elastomers (TPE) are a material group with diverse application across many industrial sectors, though components are typically manufactured via injection moulding [7]. Emerging AM capability means high-quality TPE parts can now be achieved using fused filament fabrication (FFF) [8], laser sintering [9,10] and digital light synthesis [11].

Lattice structures are strut- or surface-based geometries that enable optimised design relative to an objective function [12,13]. The former is created by struts connecting nodes arranged in three-dimensional space, with some structures resembling crystalline models including body-centred cubic, face-centre cubic, and diamond. Surface-based structures are typically more complex and often generated by mathematically- or parametrically-driven scripts [14,15]. Common examples include triply periodic minimal surface models (TPMS) - non-self-intersecting and continuously curved geometries, or origami-inspired structures with a series of flat, folded surfaces [10,16,17].

AM-built complex geometries are now produced as functional components, with numerous quasi-static compression studies describing their relative energy absorption [18–22]. Combining complex geometries and TPE materials creates new opportunities for application including helmet liners [10,23], shoe soles [11,24] and other mechanical shock absorption and actuation devices [25–27]. Whilst developing strain-rate dependent material models to achieve computational-based investigation remains technically challenging [28–30], they have enabled design of functionally graded structure to achieve a desired

* Corresponding author.
E-mail address: shwe.soe@uwe.ac.uk (S. Soe).

https://doi.org/10.1016/j.addma.2021.101885
Received 30 September 2020; Received in revised form 18 December 2020; Accepted 1 February 2021
Available online 4 February 2021
2214-8604/© 2021 The Authors. Published by Elsevier B.V. This is an open access article under the CC BY license (http://creativecommons.org/licenses/by/4.0/).

mechanical response [31–33]. Such complex structures are attained by relying on the principle of field-driven design and related physical phenomenon [34,35] out-performing a uniform lattice structure, by minimising weight and maximising stiffness; however, building very thin walls remains challenging for some AM processes [36–38].

Leveraging additional, tunable performance could also be achieved by integrating functional grading, or multiple materials, within an AM part [39–41]. Here, we introduce a new surface-based, 'closed' cell lattice that can encapsulate a second material and enables complex behaviours e.g. a biphasic response. This study aims to understand the complex interaction between the solid walls and water infill, to create new and exciting research opportunities, initially within an impact environment. This will be achieved by computationally investigating fluid deposited within a single, closed cell, with experimental validation enabled via FFF manufacturing [42,43].

2. Materials and methods

2.1. Materials

A hollow conical structure (40 mm diameter base, 35.8 mm height, 1.6 mm wall thickness) was designed in Solidworks computer aided design (CAD) software (Fig. 1a–d). This geometry was selected as having minimal overhang to ensure high quality FFF manufacture, whilst also producing a stiff and hermetic response during impact loading. Whilst these dimensions produced a cell size greater than a typical lattice structure (nominally <10 mm^3), it created an inner cavity that could contain a large fluid volume.

An FFF printer (2017 Flashforge Creator Pro printer) retrofitted with high-specification extrusion control (Diabase Engineering, USA), was tuned to fabricate the conical structure from NinjaFlex (NinjaTek, US), a readily available TPE filament (Fig. 1e). Simplify3D (Simplify3D, US) was used to define print settings and slice the STL files. The concentric infill pattern was adopted at 100% and the extrusion settings (Table 1) tuned to achieve fully dense walls without voids, which has been validated in a previous study using micro-computer tomography [8]. The g-code was modified such that a brief pause occurred at the tip of the conical geometry before the cell was closed. Water was introduced during the pause using pipette which defined the administered volume. Printing was resumed and the specimen was sealed over with subsequent layers of material, ultimately creating a 100% water-filled cone, a 70% water-filled cone and a 100% air-filled cone. A polyvinyl acrylate coating was then applied to the outer surface.

Table 1
Defines the printer parameters used for this study.

Nozzle diameter	0.4 mm
Print speed	2000 mm/min
Bed temperature	40 °C
Extruder temperature	210 °C
Extrusion multiplier	1.4
Layer height	0.1 mm
Active cooling	Yes
Infill extrusion width	125%

2.2. Experimental methods

Impact testing was conducted using a spring-loaded linear impactor (mass = 4.1 kg), guided by two solid rails (Instron Dynatup 9250 HV). An impactor with a nominal diameter of 130 mm and manufactured from tool steel was used to strike each sample. The impact speeds were chosen as 1 m/s, 2 m/s and 3 m/s, with events measured using a 500 g linear single-axis accelerometer, securely attached to the drop mass. The accelerometer was connected to a StrainStart® 9000 data acquisition system (sampling rate = 50 kHz). Raw impact data was processed using exponential smoothing analysis with a damping factor of 0.9 (MS Excel, Washington, US).

2.3. Computational methods

2.3.1. Model preparation

The above CAD geometry was exported to Abaqus finite element analysis (FEA) solver as a STEP file and a surface model (representing the mid-plane of the solid model). This enabled investigation of computational efficiency and effectiveness. The solid model's inner cavity was also created in CAD and exported to Abaqus, representing the experimental model 100% filled with either water or air. This model was equally divided in the z-height, to create the 70% water model. An upper and lower platen were then formed as two analytically rigid shells, to simulate dynamic compression. The upper platen had a 4.1 kg mass and contacted the cone's highest node, which subsequently served as the point for displacement measurement and for computing the acceleration-time response. Impact velocities were assigned to enable explicit, dynamic analysis, with the lower platen fully constrained.

The solid model was assigned quadratic tetrahedral elements (C3D10M) and meshed with ~ 2 mm global element size. The shell model was assigned 1 mm linear quadrilateral (S4R) and linear triangular (S3R) elements. Following the mesh sensitivity study the filled

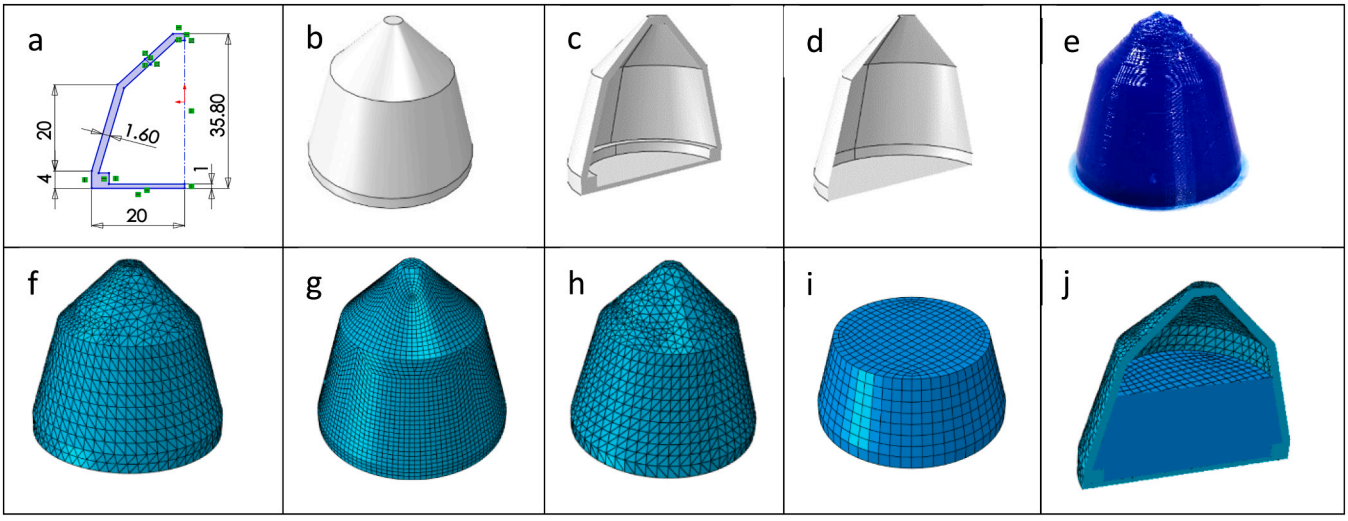

Fig. 1. Fluid-filled conical model: (a) 2D sketch with dimensions; (b) 3D solid model; (c) cut-away view of solid model; (d) cut-away view of shell model; (e) FFF part; (f) meshed solid; (g) meshed shell; (h) meshed water-filled; (i) meshed 70% water; and (j) cut-away view of meshed solid and 70% water assembly.

model was assigned 2 mm linear tetrahedron (C3D4) and the 70%-filled model linear hexagonal (C3D8R), elements. Meshing was not required for analytical rigid shells. General contact was defined for all the models. The choice of elements was governed by the intricacy of shell or solid geometry, the severity of strain gradients, the possibility of element distortion, and the complexity of contact conditions. All analyses assumed a hard contact and smooth (i.e. frictionless) interactions. For all water models, the volume mesh was converted into continuum pseudo-particles that were modelled using PC3D elements during the analysis.

2.3.2. Material assignment

The solid and shell models were assigned an hyperelastic (Mooney-Rivlin) augmented with a linear viscoelastic (Prony series) model (Table 2) [10].

Three computational methods were considered for fluid (water) modelling: (1) smooth particle hydrodynamic (SPH); (2) coupled Eulerian Lagrangian (CEL), and; (3) surface-based, fluid-filled cavity modelling [44]. SPH modelling was selected to simulate the fluid response during impact, as it achieved favourable computational time versus CEL. The water was treated as a nearly incompressible, nearly inviscid Newtonian fluid, which was modelled using the linear U_s-U_p Hugoniot form of the Mie-Grüneisen equation of state. The equation parameters appear in Table 3 [44].

The 100% air-filled cell was modelled by creating a surface-based fluid-filled cavity. In this approach the cavity reference node and an element-based surface were defined on the inside of the cone. This surface was used to define a fluid cavity filled with air. This cavity reference node has a single degree of freedom representing the pressure inside the fluid cavity. The finite element calculations for surface-based cavities were performed using volume elements, which were created internally by Abaqus using the surface facet geometry and the cavity reference node. In Table 4, the air properties from inside the cone are defined as part of the fluid behaviour [44]. All simulations were performed using parallel processing capability afforded by Intel®Core™i9-9980HK CPU@2.40 GHz processor, 32 GB RAM, 64-bit operating system where each simulation was allocated with 4 multiple processors.

3. Result and discussion

3.1. Experimental evaluation

The acceleration-time responses of the 3 conical structures (100% water-, 70% water- and 100% air-filled) impacted at 3 different velocities (1, 2 and 3 m/s) are presented in Fig. 2.

At 1 m/s, all structures achieve a similar plateau response up to 0.01 s, followed by rapid acceleration (Fig. 2a). The 100% air-filled model then has a 6 g-force (g) peak at 0.015 s, maintained until 0.025 s, before reducing. The overall time impulse is 0.04 s. The 100% water-filled model records a 9 g peak acceleration, maintained for a shorter impulse period and recording 0.035 s overall impact time. The 70% water-filled model follows a similar response as the 100% air-filled model to 6 g, then linearly increases to 9 g, before the acceleration is reduced. This means the 70% water-filled model demonstrates behaviour between the two other constructs.

At 2 m/s impact speed (Fig. 2b), the sharp peaks of the acceleration-time profiles indicate models entered the densification phase. At this impact condition, the 100% air-filled (33 g) exhibited superior performance. The 70% and 100% water-filled model had 48 g and 42 g peak accelerations, respectively. These peak accelerations are much higher than the slower impact speeds, with shorter time durations.

Increasing impact speed to 3 m/s (Fig. 2c), the 100% air-filled model then generated the highest peak acceleration (108 g), versus 70% water-filled (97 g) and 100% water-filled (82 g). This means fluid-filled structures are more effective at dissipating relatively high impact energies, versus contemporary air-filled structures. All 3 m/s models again have a much shorter impulse (0.02 s) than the slower impacts.

Table 2
TPE visco-hyperelastic model parameters [10].

Mooney-Rivlin material model coefficients		Viscoelasticity Prony series			
C10/MPa	C01/MPa		G/MPa	K/MPa	tau/s
2.93	0.363	1	0.196	0.00	1.27E-03
		2	0.129	0.00	8.30E-02
		3	7.67E-02	0.00	0.894
		4	6.03E-02	0.00	6.51
		5	7.10E-02	0.00	54.6

Table 3
Water properties and values used in FEA simulation.

Parameters	Value	Units
Density (ρ)	1×10^{-9}	Tonne/mm^3
Viscosity (η)	1×10^{-9}	MPa s
Speed of sound (c_0)	1.48×10^6	mm/s
S	0	
Γ_0	0	

Table 4
Air properties and values used in FEA simulation.

Parameters	Value	Units
Absolute zero temperature	−273	°C
Universal gas constant	8314	mJ/mol K
Ideal gas molecular weight (air weight in the cavity)	8.09×10^{-9}	tonne
Molar heat capacity (air heat capacity at constant pressure)	29.19×10^3	mJ/mol K
Ambient pressure (pressure inside the cavity)	0.1	MPa

3.2. FEA evaluation

FEA simulations were performed to better understand the fluid-structure experimental interactions. The shell and solid models also enabled consideration of the most appropriate computational approach to simulate these complex problems.

The 1 m/s simulated impact impulse (Fig. 3) was replicated from the experimental setup. The computationally derived acceleration-time trace for the 100% water-filled model exhibited close correlation with the experimental data. A positive correlation was evident for the peak acceleration and pulse duration for the 70% water-filled solid and shell simulations, though both under-predicted the compression phase by 0.01–0.02 s. The 100% air-filled models both underpredicted the peak value, whilst the computational impulse time was longer than the experimental data in the energy releasing phase. This rebound inaccuracy could be influenced by the absence of the Mullins effect material model, which considers the hysteresis loading and unloading for a given cycle following different paths. A similar phenomenon was observed in a previous study, especially at lower impact velocities [10]. Improved fidelity, however, is observed for higher impact energies as shown in Figs. 4c and 6c.

Acceleration-time traces for the 2 m/s water-filled impact (Fig. 4) indicates close comparability between the solid model and experimental data. Whilst the shell model slightly overpredicted peak g, when considering its reduced computational time versus the solid model (Fig. 7), this approach appears to quickly achieve reasonably accurate data, when investigating complex geometries. Both the solid and shell 100% air-filled simulations overpredicted peak g, though the former was more accurate in forecasting impulse time. The upper platen displacement was also compared between the experiment and simulations (Fig. 4d). All analytical solutions demonstrated a linear displacement before reaching maximum compression. The air-filled solid simulation has the strongest correlation with equivalent experimental data (0.4%

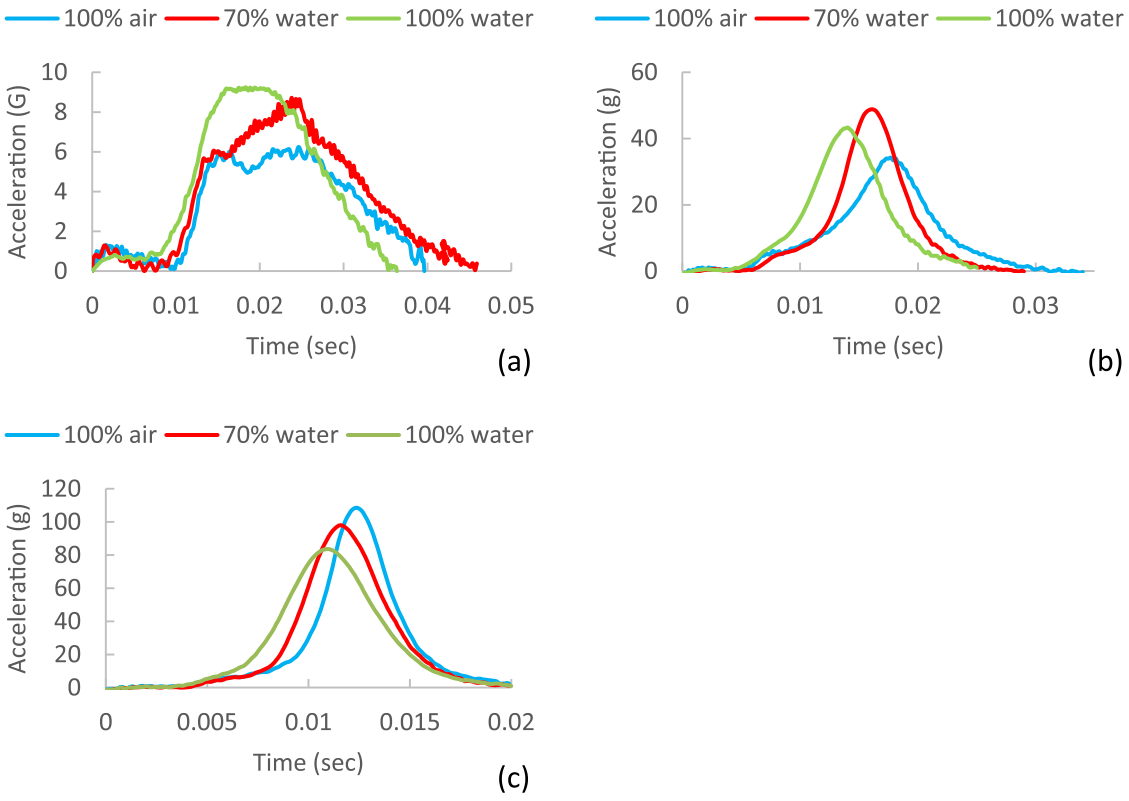

Fig. 2. Acceleration-time responses of 100% water-filled, 70% water-filled and 100% air-filled structures impacted at (a) 1 m/s, (b) 2 m/s, and (c) 3 m/s.

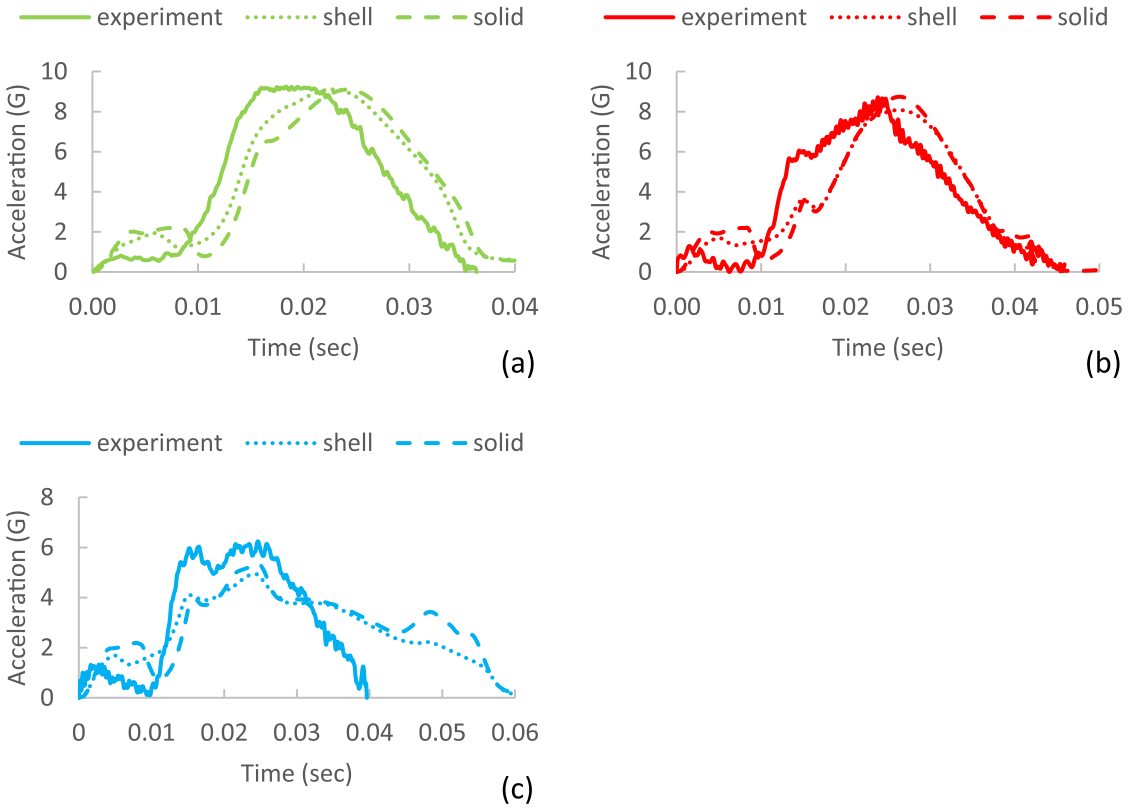

Fig. 3. Experimental and simulated acceleration-time graphs for 1 m/s impact speed (a) 100% water-filled, (b) 70% water-filled, (c) 100% air-filled.

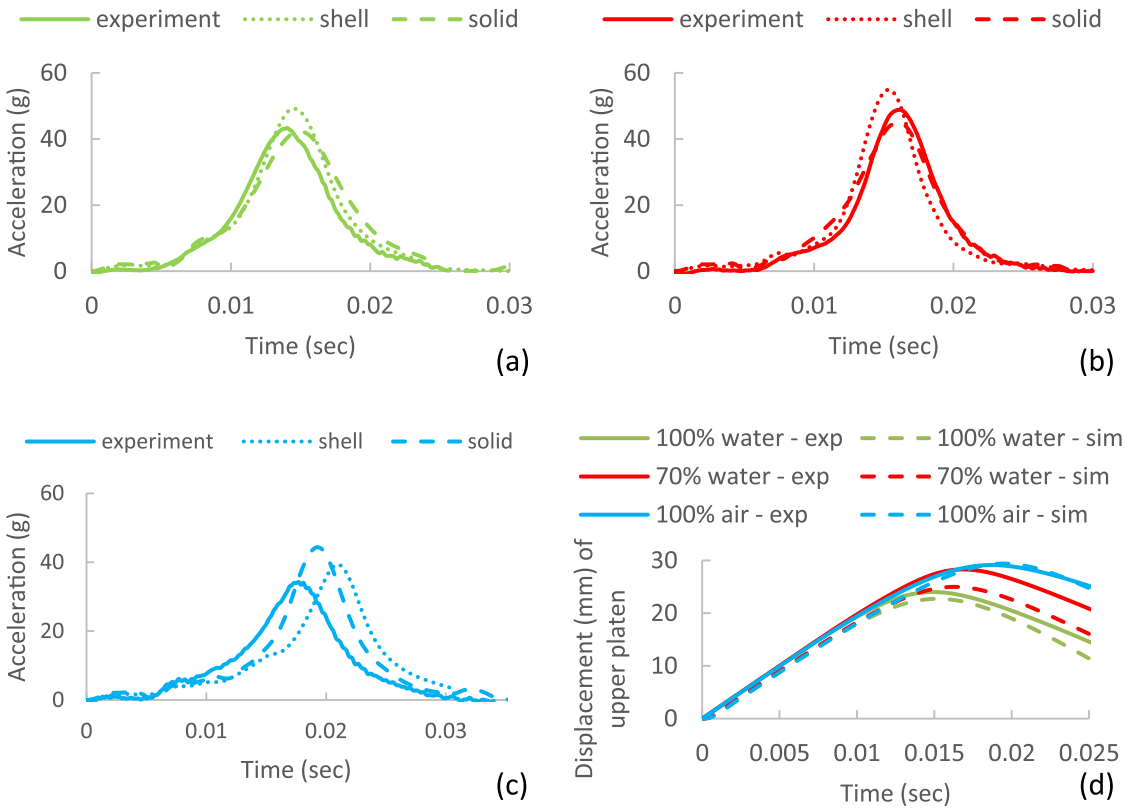

Fig. 4. Experimental and simulated acceleration-time graphs describing a 2 m/s impact on a conical structure that was (a) 100% water-filled, (b) 70% water-filled and, (c) 100% air-filled. (d) Upper platen displacement trends.

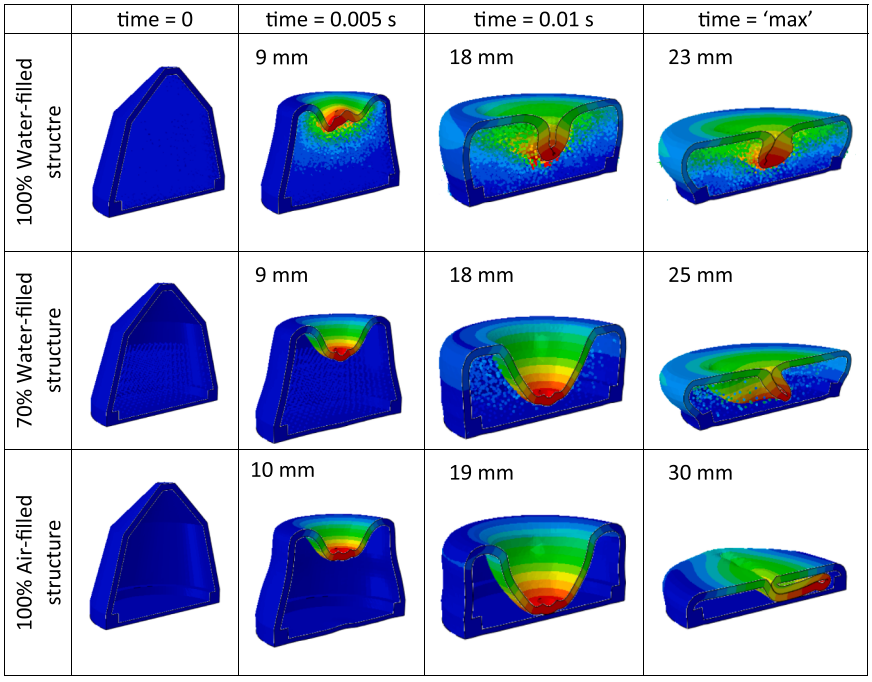

Fig. 5. Compression response of the 3 models at t = 0 s, 0.005 s, 0.01 s and 'max'. The additional values describe the minimum deflection, calculated as the difference between the original height and the highest remaining feature. The particles represent water.

deviation), then the 100% water-filled models (0.5% deviation). The 70% water-filled model over-predicted deflection by 12%.

Cut-away views of all models demonstrate the relative structural deformation and fluid displacement (Fig. 5) at t = 0 s, 0.005 s, 0.01 s and maximum (i.e. time at peak) (Fig. 4). All models show similar compression responses from t = 0 s to t = 0.01 s (Fig. 4d). Fig. 5 describes numerical differences in the physical collapse behaviours. At t = 0.005 s, the maximum side wall deflection is 9–10 mm across all

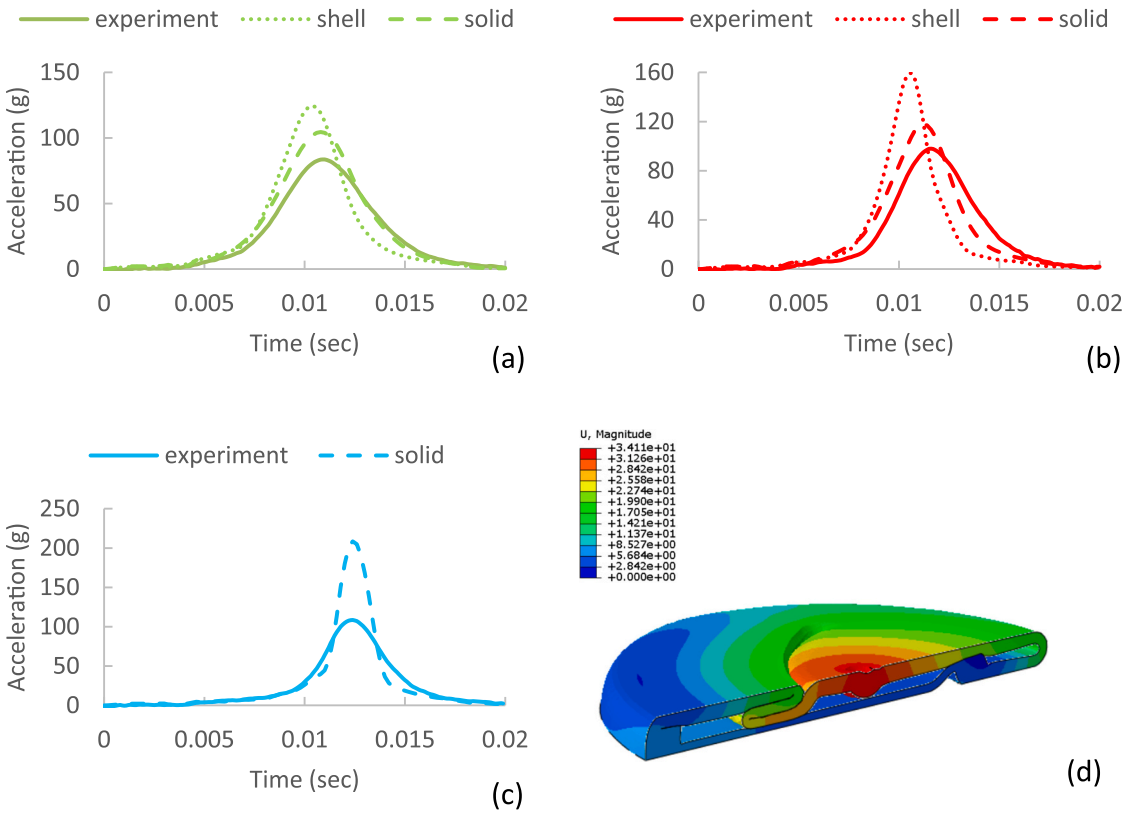

Fig. 6. Experimental and simulated acceleration-time graphs for 3 m/s impact speed (a) 100% water-filled, (b) 70% water-filled, (c) 100% air-filled structures, (d) Cut-away view of fully compressed air-filled model.

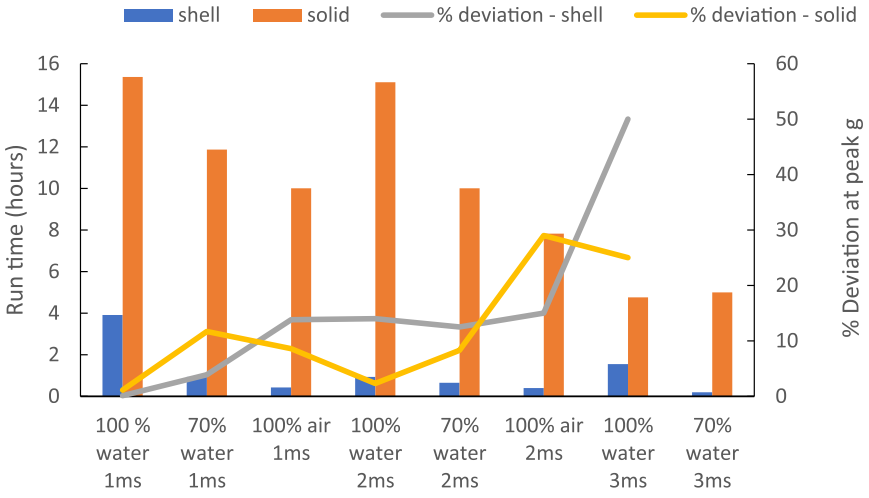

Fig. 7. Run time efficiency and % deviation at peak g between solid and shell models for 3 impact velocities.

tests, though the mechanism of collapse appears dependant on fluid resistance. This deflection is initiated by cell wall buckling, which is visible on some acceleration-time plots as an initial peak that appears dependant on both loading rate and infill. At t = 0.01 s, the maximum side wall deflection was 18–19 mm across all models. In this case the difference is more pronounced; the top portion of the air-filled model begins contacting the base; however, no contact is evident in the other models. The final time-step, t = max, represents maximum deformation in each model. As expected, the 100% air-filled structure is completely folded given the lowest fluid resistance, whereas the 70% water-filled and 100% water-filled models demonstrate less deformation. All such scenarios do, however, represent a point of relative densification and so create a second, larger, peak acceleration (Figs. 2–6).

Fig. 6(a and b) compare the experimental and simulation output of the 100% water-filled and 70% water-filled structures, at a 3 m/s impact speed. The impulse responses from both solid and shell solutions were close to the equivalent experimental data; however, the latter significantly over-predicted peak g. The air-filled simulation data (Fig. 6c) is presented for the solid model only, as the shell simulation failed due to increased inter-surface penetration. Peak g is far greater in the numerical solution (relative to the experimental data), caused by poor fidelity of the visco-hyperelastic material model in full-densification scenarios (Fig. 6d). This highlights that shell modelling, whilst computationally cheaper, is unsuitable for scenarios with multiple, complex surfaces,

where there is a densification risk.

3.3. Run-time efficiency

The shell and solid model processing time for all impact velocities are shown in Fig. 7, together with the percentage deviation between experiment and simulation peak g result. Solid model processing times ranged from 5 to 15.5 h, depending on the allocated impulse times. Shell processing times ranged from 0.19 to 4 h. The percentage deviations at peak g are comparable for 1 m/s and 2 m/s impact velocities for shell and solid models. The difference is more pronounced at 3 m/s, however, with the results clearly indicating that solid modelling is a necessity for final validation, although the shell model does afford some time-saving during the initial design optimisation phase. The transition from shell to solid model will, however, ultimately be governed by the accuracy demanded for each design scenario.

4. Conclusion

This study aimed to understand how a fluid-filled, closed-cell structure could reduce acceleration during impact. Experimental data demonstrates fluid influences and reduces acceleration and so can be considered to improve protective performance, relative to contemporary, air-filled structures at higher impact energies. This could be important in structures where energy absorption is of critical importance.

This work also provides a computational pathway to efficiently and effectively developing new and novel fluid-filled structures. The SPH and fluid-based air-cavity computational techniques were successfully employed for water and air, respectively. At low to medium impact loading, shell and solid modelling accurately simulated experimental trends, although the latter was more computationally expensive. Solid modelling is the only viable solution for higher impacts causing structural densification, as inter-surface penetrations cause inaccuracies in shell-based models.

CRediT authorship contribution statement

Shwe Soe: Conceptualization, Methodology, Validation, Formal analysis, Investigation, Writing - original draft, Visualization. **Rhosslyn Adams**: Methodology, Investigation, Writing - review & editing. **Mokarram Hossain**: Conceptualization, Writing - review & editing. **Peter Theobald**: Conceptualization, Writing - review & editing, Project administration, Funding acquisition.

Declaration of Competing Interest

The authors declare that they have no known competing financial interests or personal relationships that could have appeared to influence the work reported in this paper.

Acknowledgements

This study was supported by funding from Cardiff University's EPSRC Impact Accelerator Account and Research Opportunities Programme.

References

[1] S.K. Everton, M. Hirsch, P. Stravroulakis, R.K. Leach, A.T. Clare, Review of in-situ process monitoring and in-situ metrology for metal additive manufacturing, Mater. Des. 95 (2016) 431–445.
[2] M. Borish, B.K. Post, A. Roschli, P.C. Chesser, L.J. Love, Real-time defect correction in large-scale polymer additive manufacturing via thermal imaging and laser profilometer, Procedia Manuf. 48 (2020) 625–633.
[3] S.A. Shevchik, C. Kenel, C. Leinenbach, K. Wasmer, Acoustic emission for in situ quality monitoring in additive manufacturing using spectral convolutional neural networks, Addit. Manuf. 21 (2018) 598–604.
[4] N. Li, S. Huang, G. Zhang, R. Qin, W. Liu, H. Xiong, G. Shi, J. Blackburn, Progress in additive manufacturing on new materials: a review, J. Mater. Sci. Technol. 35 (2) (2019) 242–269.
[5] C.M. González-Henríquez, M.A. Sarabia-Vallejos, J. Rodriguez-Hernandez, Polymers for additive manufacturing and 4D-printing: materials, methodologies, and biomedical applications, Prog. Polym. Sci. 94 (2019) 57–116.
[6] S. Yuan, F. Shen, C.K. Chua, K. Zhou, Polymeric composites for powder-based additive manufacturing: Materials and applications, Prog. Polym. Sci. 91 (2019) 141–168.
[7] The Future of Thermoplastic Elastomers to 2024, https://www.smithers.com/en-gb/services/market-reports/materials/the-future-of-thermoplastic-elastomers-to-2024. (Accessed 27 August 2020).
[8] M. Robinson, S. Soe, R. Johnston, R. Adams, B. Hanna, R. Burek, G. McShane, R. Celeghini, M. Alves, P. Theobald, Mechanical characterisation of additively manufactured elastomeric structures for variable strain rate applications, Addit. Manuf. 27 (2019) 398–407.
[9] S.P. Soe, N. Martindale, C. Constantinou, M. Robinson, Mechanical characterisation of Duraform® Flex for FEA hyperelastic material modelling, Polym. Test. 34 (2014) 103–112.
[10] R. Adams, S.P. Soe, R. Santiago, M. Robinson, B. Hanna, G. McShane, M. Alves, R. Burek, P. Theobald, A novel pathway for efficient characterisation of additively manufactured thermoplastic elastomers, Mater. Des. 180 (2019), 107917.
[11] M. Hossain, Z. Liao, An additively manufactured silicone polymer: thermo-viscoelastic experimental study and computational modelling, Addit. Manuf. 35 (2020), 101395.
[12] I. Maskery, A.O. Aremu, L. Parry, R.D. Wildman, C.J. Tuck, I.A. Ashcroft, Effective design and simulation of surface-based lattice structures featuring volume fraction and cell type grading, Mater. Des. 155 (2018) 220–232.
[13] L. Yang, C. Yan, C. Han, P. Chen, S. Yang, Y. Shi, Mechanical response of a triply periodic minimal surface cellular structures manufactured by selective laser melting, Int. J. Mech. Sci. 148 (2018) 149–157.
[14] M. Zhao, D.Z. Zhang, F. Liu, Z. Li, Z. Ma, Z. Ren, Mechanical and energy absorption characteristics of additively manufactured functionally graded sheet lattice structures with minimal surfaces, Int. J. Mech. Sci. 167 (2020), 105262.
[15] B. Hanks, J. Berthel, M. Frecker, T.W. Simpson, Mechanical properties of additively manufactured metal lattice structures: data review and design interface, Addit. Manuf. 35 (2020), 101301.
[16] J.A. Harris, G.J. McShane, Metallic stacked origami cellular materials: additive manufacturing, properties, and modelling, Int. J. Solids Struct. 185 (2020) 448–466.
[17] S. Townsend, R. Adams, M. Robinson, B. Hanna, P. Theobald, 3D printed origami honeycombs with tailored out-of-plane energy absorption behavior, Mater. Des. 195 (2020), 108930.
[18] Y. Xu, D. Zhang, S. Hu, R. Chen, Y. Gu, X. Kong, J. Tao, Y. Jiang, Mechanical properties tailoring of topology optimized and selective laser melting fabricated Ti6Al4V lattice structure, J. Mech. Behav. Biomed. Mater. 99 (2019) 225–239.
[19] T. Maconachie, M. Leary, B. Lozanovski, X. Zhang, M. Qian, O. Faruque, M. Brandt, SLM lattice structures: properties, performance, applications and challenges, Mater. Des. 183 (2019), 108137.
[20] Q. Feng, Q. Tang, Y. Liu, R. Setchi, S. Soe, S. Ma, L. Bai, Quasi-static analysis of mechanical properties of Ti6Al4V lattice structures manufactured using selective laser melting, Int. J. Adv. Manuf. Technol. 94 (5–8) (2018) 2301–2313.
[21] I. Maskery, L. Sturm, A.O. Aremu, A. Panesar, C.B. Williams, C.J. Tuck, R. D. Wildman, I.A. Ashcroft, R.J. Hague, Insights into the mechanical properties of several triply periodic minimal surface lattice structures made by polymer additive manufacturing, Polymer 152 (2018) 62–71.
[22] F.N. Habib, P. Iovenitti, S.H. Masood, M. Nikzad, Fabrication of polymeric lattice structures for optimum energy absorption using multi jet fusion technology, Mater. Des. 155 (2018) 86–98.
[23] S.P. Soe, P. Martin, M. Jones, M. Robinson, P. Theobald, Feasibility of optimising bicycle helmet design safety through the use of additive manufactured TPE cellular structures, Int. J. Adv. Manuf. Technol. 79 (9–12) (2015) 1975–1982.
[24] https://carbon3d.com/resources/case-study/adidas/. (Accessed 27 August 2020).
[25] J. Brennan-Craddock, D. Brackett, R. Wildman, R. Hague, The design of impact absorbing structures for additive manufacture, J. Phys. Conf. Ser. 382 (1) (2012), 012042.
[26] W.P. Syam, W. Jianwei, B. Zhao, I. Maskery, W. Elmadih, R. Leach, Design and analysis of strut-based lattice structures for vibration isolation, Precis. Eng. 52 (2018) 494–506.
[27] C.J. Hohimer, G. Petrossian, A. Ameli, C. Mo, P. Pötschke, 3D printed conductive thermoplastic polyurethane/carbon nanotube composites for capacitive and piezoresistive sensing in soft pneumatic actuators, Addit. Manuf. 34 (2020), 101281.
[28] X. Cao, D. Xiao, Y. Li, W. Wen, T. Zhao, Z. Chen, Y. Jiang, D. Fang, Dynamic compressive behavior of a modified additively manufactured rhombic dodecahedron 316L stainless steel lattice structure, Thin Walled Struct. 148 (2020), 106586.
[29] S. Adhikari, T. Mukhopadhyay, A. Shaw, N.P. Lavery, Apparent negative values of Young's moduli of lattice materials under dynamic conditions, Int. J. Eng. Sci. 150 (2020), 103231.
[30] C. Ling, A. Cernicchi, M.D. Gilchrist, P. Cardiff, Mechanical behaviour of additively-manufactured polymeric octet-truss lattice structures under quasi-static and dynamic compressive loading, Mater. Des. 162 (2019) 106–118.
[31] D. Qi, Q. Lu, C. He, Y. Li, W. Wu, D. Xiao, Impact energy absorption of functionally graded chiral honeycomb structures, Extrem. Mech. Lett. 32 (2019), 100568.

[32] L. Bai, C. Gong, X. Chen, Y. Sun, L. Xin, H. Pu, Y. Peng, J. Luo, Mechanical properties and energy absorption capabilities of functionally graded lattice structures: experiments and simulations, Int. J. Mech. Sci. 182 (2020), 105735.
[33] S. Yu, J. Sun, J. Bai, Investigation of functionally graded TPMS structures fabricated by additive manufacturing, Mater. Des. 182 (2019), 108021.
[34] https://ntopology.com/field-driven-design/. (Accessed 31 August 2020).
[35] G. Dong, Y. Tang, D. Li, Y.F. Zhao, Design and optimization of solid lattice hybrid structures fabricated by additive manufacturing, Addit. Manuf. 33 (2020), 101116.
[36] P.M. Bhatt, R.K. Malhan, P. Rajendran, S.K. Gupta, Building free-form thin shell parts using supportless extrusion-based additive manufacturing, Addit. Manuf. 32 (2020), 101003.
[37] A. Arjunan, M. Singh, A. Baroutaji, C. Wang, Additively manufactured AlSi10Mg inherently stable thin and thick-walled lattice with negative Poisson's ratio, Compos. Struct. 247 (2020), 112469.
[38] T. Romeijn, B. Wells, D. Wei, G. Paul, Investigation into the shear property of thin-walled additively manufactured structures using staggered fused filament fabrication, Addit. Manuf. 35 (2020), 101259.
[39] B. Saleh, J. Jiang, R. Fathi, T. Al-hababi, Q. Xu, L. Wang, D. Song, A. Ma, 30 Years of functionally graded materials: an overview of manufacturing methods, applications and future challenges, Compos. Part B Eng. 201 (2020), 108376.
[40] G.H. Loh, E. Pei, D. Harrison, M.D. Monzon, An overview of functionally graded additive manufacturing, Addit. Manuf. 23 (2018) 34–44.
[41] F. Liu, T. Li, X. Jiang, Z. Jia, Z. Xu, L. Wang, The effect of material mixing on interfacial stiffness and strength of multi-material additive manufacturing, Addit. Manuf. 36 (2020), 101502.
[42] J. Yin, C. Lu, J. Fu, Y. Huang, Y. Zheng, Interfacial bonding during multi-material fused deposition modeling (FDM) process due to inter-molecular diffusion, Mater. Des. 150 (2018) 104–112.
[43] D.J. Roach, C.M. Hamel, C.K. Dunn, M.V. Johnson, X. Kuang, H.J. Qi, The m4 3D printer: a multi-material multi-method additive manufacturing platform for future 3D printed structures, Addit. Manuf. 29 (2019), 100819.
[44] SIMULIA User Assistance Online Documentation, 2019.